The Astrophysical Journal, 791:124 (13pp), 2014 August 20 doi:10.1088/0004-637X/791/2/124

FILAMENTS IN SIMULATIONS OF MOLECULAR CLOUD FORMATION

Gilberto C. Gómez and Enrique Vázquez-Semadeni
Centro de Radioastronomía y Astrofísica, Universidad Nacional Autónoma de México, Campus Morelia Apartado Postal 3-72, 58090 Morelia, Michoacán, Mexico
Received 2013 August 26; accepted 2014 July 17; published 2014 August 6

ABSTRACT

We report on the filaments that develop self-consistently in a new numerical simulation of cloud formation by colliding flows. As in previous studies, the forming cloud begins to undergo gravitational collapse because it rapidly acquires a mass much larger than the average Jeans mass. Thus, the collapse soon becomes nearly pressureless, proceeding along its shortest dimension first. This naturally produces filaments in the cloud and clumps within the filaments. The filaments are not in equilibrium at any time, but instead are long-lived flow features through which the gas flows from the cloud to the clumps. The filaments are long-lived because they accrete *from* their environment while simultaneously accreting *onto* the clumps within them; they are essentially the locus where the flow changes from accreting in two dimensions to accreting in one dimension. Moreover, the clumps also exhibit a hierarchical nature: the gas in a filament flows onto a main, central clump but other, smaller-scale clumps form along the infalling gas. Correspondingly, the velocity along the filament exhibits a hierarchy of jumps at the locations of the clumps. Two prominent filaments in the simulation have lengths $\sim$15 pc and masses $\sim$600 $M_\odot$ above density $n \sim 10^3$ cm^{-3} ($\sim 2\times10^3$ $M_\odot$ at $n > 50$ cm^{-3}). The density profile exhibits a central flattened core of size $\sim$0.3 pc and an envelope that decays as $r^{-2.5}$ in reasonable agreement with observations. Accretion onto the filament reaches a maximum linear density rate of $\sim$30 $M_\odot$ Myr^{-1} pc^{-1}.

Key words: evolution – ISM: clouds – stars: formation

Online-only material: animations, color figures

1. INTRODUCTION

Filamentary structure is ubiquitous in molecular clouds, both actively star forming and quiescent (e.g., Bally et al. 1987; Feitzinger et al. 1987; Gutermuth et al. 2008; Myers 2009; Juvela et al. 2009; André et al. 2010; Henning et al. 2010; Men'shchikov et al. 2010; Molinari et al. 2010; Schneider et al. 2010; Arzoumanian et al. 2011; Kirk et al. 2013). Moreover, these works have shown that regardless of whether the filaments are actively forming stars or not, they often contain dense clumps and cores which may or may not harbor young stellar objects. If not, the cores are labeled "prestellar."

Numerous physical mechanisms have been advocated for the formation of the filaments, such as the gravitational instability of a flattened isothermal cloud, with and without magnetic fields (e.g., Larson 1985; Miyama et al. 1987; Gehman et al. 1996; Nagai et al. 1998; Curry 2000; Balsara et al. 2001); supersonic MHD isothermal turbulence (e.g., Padoan et al. 2001; Goldsmith et al. 2008; Padoan et al. 2001); and turbulence in thermally unstable gas (e.g., Klein & Woods 1998; Vázquez-Semadeni et al. 2006; Walder & Folini 2000; Pavlovski et al. 2002). However, recent numerical simulations of cloud formation and evolution including self-gravity systematically show that the clouds, rather than remaining globally supported by turbulence, engage in global gravitational contraction (e.g., Burkert & Hartmann 2004; Hartmann & Burkert 2007; Vázquez-Semadeni et al. 2007, 2009, 2011; Heitsch & Hartmann 2008; Heitsch et al. 2008; Banerjee et al. 2009; Carroll-Nellenback et al. 2013).[1] These results suggest that although the interstellar medium is highly turbulent, the dynamics and structure of star-forming molecular clouds, and the filaments within them, may actually be dominated by gravity.

That cold clouds may be in a state of global gravitational contraction should not come in as a surprise, since the formation mechanism of cold clouds may quickly endow them with masses much larger than their Jeans mass. Indeed, cold clouds are expected to form, at least in solar-neighborhood-like environments, by means of large-scale, coherent compressions in the warm neutral medium (WNM), driven, for example, by large (kpc)-scale instabilities (Jeans, Toomre, Parker, and combinations thereof; e.g., Elmegreen 1987; Kim et al. 2002), or else by the generic turbulence in this medium, which is typically transonic (e.g., Heiles & Troland 2003). Such compressions in the WNM are expected to induce a sudden phase transition to the cold neutral medium[2] (CNM; e.g., Hennebelle & Pérault 1999; Koyama & Inutsuka 2000, 2002; Heitsch et al. 2005;

[1] There have been some claims in the literature that the molecular clouds may be gravitationally unbound (e.g., Dobbs et al. 2011). However, closer examination of the evidence suggests that the clouds may become unbound as a consequence of the stellar feedback (see the discussion by Colín et al. 2013), so that the unbound stage is a *late* state of the clouds, while here we are interested in the *initial* conditions in the clouds.

[2] Note that this mechanism is not in contradiction with the fact that observations (e.g., Dickey et al. 1977; Kalberla et al. 1985; Spitzer & Fitzpatrick 1995; Heiles & Troland 2003; Jenkins & Tripp 2011) as well as simulations (e.g., Vázquez-Semadeni et al. 2000; Gazol et al. 2001, 2005; de Avillez & Breitschwerdt 2004; Wada & Norman 2007; Tasker & Bryan 2008) systematically show that the density, temperature, and pressure in the ISM span a continuum rather than being restricted to narrow ranges of values, as in the classical multi-phase models (Field et al. 1969; McKee & Ostriker 1977). As discussed by Vázquez-Semadeni et al. (2006), the flow may *locally* undergo such phase transitions whenever it is subject to compressions that push it out of thermal equilibrium, creating condensation fronts that separate cold clouds from their warm, diffuse environment. However, because there are significant pressure fluctuations throughout the medium, the phase transitions will occur around different mean pressures, and therefore the physical conditions of the local warm and cold phases will differ from those of the corresponding phases at a different location, producing a statistical continuum of densities and temperatures (Vázquez-Semadeni 2012b). Moreover, Banerjee et al. (2009) showed that at some locations the boundaries between the cold and warm phases are rather sharp, while at other locations they are significantly smoother, depending on the local turbulent conditions, again producing significant amounts of thermally unstable gas which populates the density PDF in the classically forbidden regimes.

Vázquez-Semadeni et al. 2006), which has a density roughly 100× larger and a temperature roughly 100× lower than those of the WNM. Thus, the Jeans mass, proportional to $\rho^{-1/2}T^{3/2}$, drops by a factor $\sim 10^4$, and so the gas can easily acquire a large number of Jeans masses upon the phase transition from the warm to the cold phase. This implies that the ensuing collapse must occur in an essentially pressureless manner. However, if the collapse occurs in a nearly pressureless form, an important consequence follows: as the collapse proceeds, it is expected to amplify any deviations from isotropy since it has been known for a long time that pressureless triaxial spheroids collapse first along their shortest dimension (Lin et al. 1965), producing first sheets and then filaments.

Interestingly, the formation of structures in cold, dense clouds may be qualitatively similar to that in the so-called cosmic web, which is believed to be permeating intergalactic space (e.g., Bond et al. 1996; Cantalupo et al. 2014) and which consists of a network of filaments with dense galaxy clusters within them. In the cosmic web, the filamentary structures are certainly not expected to be in equilibrium since they are actually undergoing gravitational collapse. Quite the opposite, the filaments feed material to the clusters sitting within them and play a crucial role on the evolution of the galaxies in the clusters. Since observations of nearby molecular clouds (Myers 2009) as well as recent simulations of molecular cloud formation (e.g., Vázquez-Semadeni et al. 2007, 2011; Heitsch et al. 2009; Naranjo-Romero et al. 2012) show a similar hub-filament structure, it is tempting to infer that the physical process in the cold clouds is similar as well, implying that their filamentary environment might have a strong influence on the evolution of pre-stellar cores (see also Gómez et al. 2007; Smith et al. 2012).

It is important to point out, however, that contrary to the cosmological case, a nascent cold cloud is internally turbulent due to several fluid instabilities acting during its formation process (Hunter et al. 1986; Vishniac 1994; Koyama & Inutsuka 2002; Audit & Hennebelle 2005; Heitsch et al. 2005; Vázquez-Semadeni et al. 2006). It has been thought for some time that this turbulence may be strong enough to support the clouds (e.g., Klessen & Hennebelle 2010), and to simultaneously induce local compressions in which the local Jeans mass is reduced sufficiently to cause the local fluctuation to undergo collapse (Padoan 1995; Padoan & Nordlund 2002, 2011; Vázquez-Semadeni et al. 2003a; Krumholz & McKee 2005; Hennebelle & Chabrier 2011). However, early on it was pointed out by Clark & Bonnell (2005) that, generally, the turbulent compressions alone do not provide a sufficient reduction of the local Jeans mass as to directly induce local collapse. This is supported by the fact that numerical simulations of cloud formation indicate that the turbulence generated as the cloud is assembled is only moderately, rather than strongly, supersonic (e.g., Koyama & Inutsuka 2002; Audit & Hennebelle 2005; Heitsch et al. 2005; Vázquez-Semadeni et al. 2006, 2010; Banerjee et al. 2009), and that *local* gravitational collapse does not start until several million years later in the clouds' evolution, that is, after significant contraction of the clouds at large (e.g., Vázquez-Semadeni et al. 2007, 2010; Heitsch et al. 2008).

However, once the nonlinear density fluctuations begin to collapse locally, they do so on shorter timescales than that of the whole cloud precisely because of their nonlinearly larger local density compared to the average cloud density, causing a regime of hierarchical gravitational fragmentation (i.e., of collapses within collapses; Vázquez-Semadeni et al. 2009) similar to the regime originally proposal of Hoyle (1953), except for the nonlinearity of the density fluctuations (see, e.g., the review by Vázquez-Semadeni 2012a).

Note also that, as originally pointed out by Hoyle (1953), if the collapse is nearly isothermal, then number of Jeans masses in a cloud increases as it collapses. This implies that the collapse of the cloud continues to behave as a pressure-free flow. Although the thermal pressure does indeed increase during the collapse, it is always lagging behind the gravitational energy density, and by an ever-larger margin. In this way, the collapse of a turbulent, isothermal cloud is seen to behave similarly to the collisionless dark matter fluid. Thus, it is expected to proceed by enhancing its eccentricity, effectively collapsing first along its shortest dimension, and thus forming first sheets and then filaments (Lin et al. 1965). The filaments formed by this global process are expected to be surrounded by this accretion-driven *ram* pressure and dynamically very different from filaments confined by the thermal pressure of a static medium.

Recent observational studies have emphasized the filamentary structure of molecular clouds, mainly thanks to the advent of the *Herschel* telescope, devoting special attention to the spatial and velocity structure of the filaments, and the implied accretion rates onto and along the filaments (André et al. 2010; Arzoumanian et al. 2011; Battersby et al. 2014; Hacar et al. 2013; Kirk et al. 2013; Molinari et al. 2010; Myers 2009). With this in mind, in this paper, we present a new, high-resolution numerical simulation of dense cloud formation by colliding flows, and report the physical conditions of the filaments that develop in this simulation by gravitational contraction. We have chosen this setup as it provides a self-consistent mechanism for driving the turbulence in the forming dense cloud, contrary to the case of simulations in which the turbulence is externally driven by a force generated in Fourier space and applied everywhere in the flow. The latter scheme, although quite common in the literature (e.g., Padoan & Nordlund 1999; Padoan et al. 2007; Klessen et al. 2000; Vázquez-Semadeni et al. 2003a, 2005, 2008; Kritsuk et al. 2007; Federrath & Klessen 2012, 2013), has the disadvantage that the turbulent Mach number is imposed, rather than self-consistently produced, and thus it is not possible to know whether it is realistic or not. An excessive imposed turbulent Mach number can indeed have the effect of providing global support while simultaneously inducing local collapse, eliminating the feature of global collapse, but this is likely to be an artifact of the excessive and whole-volume-application nature of the driving.

The plan of the paper is as follows. In Section 2, we present the numerical simulation and then discuss its global evolution in Section 3. Next, in Section 4, we report the physical properties and conditions in one fiducial filament that develops in the simulation. Finally, in Section 6, we present a summary and our conclusions.

2. NUMERICAL MODEL

The simulation used in this study is similar to the simulation L256Δv0.17 discussed in Vázquez-Semadeni et al. (2007, hereafter Paper I), although performed at a significantly higher resolution ($296^3 \approx 2.6 \times 10^7$ smoothed particle hydrodynamics (SPH) particles versus $148^3 \approx 3.2 \times 10^6$), and performed with the GADGET-2 code while in Paper I the code GADGET was used. The simulation describes the collision of two oppositely directed streams of warm gas. The collision triggers a transition to the cold phase, forming a cloud that rapidly grows in mass by

accretion of the warm, diffuse inflow material until it becomes Jeans unstable and begins to collapse. We refer the reader to Paper I for specific details of the setup and a description of the more general behavior. While the general behavior of the simulation is the same as in Paper I, the higher resolution causes some differences in the details of the evolution which we describe below.

The simulation was performed in a box of 256 pc per side initially filled with warm gas of uniform density ($1\,\mathrm{cm}^{-3}$) and temperature ($T = 5206$ K). The box thus contains a total mass of $5.26 \times 10^7\,M_\odot$. At our chosen number of SPH particles, assuming a mass per gas particle of $m_{\rm eff} = 2.12 \times 10^{-24}$ g, the mass per SPH particle in our simulation is $\approx 0.02\,M_\odot$.

Two cylindrical regions within this box were set to collide within this box, with initial velocities $v_{\rm inf}$ ($= 9.2\,\mathrm{km\,s}^{-1} = 1.22 c_s$, where c_s is the adiabatic sound speed), and $-v_{\rm inf}$, so that they collide at the central (y, z) plane of the box. Note that the inflows have the same density as the ambient medium, so they are only distinguished from it by their velocity, not by their density.

The dimensions of the cylinders were $l_{\rm inf} = 112$ pc and $r_{\rm inf} = 32$ pc, and thus contained $2.64 \times 10^4\,M_\odot$ each, causing the total mass in the cold cloud to be $\gtrsim 5.2 \times 10^4\,M_\odot$. Note that the mass is larger than twice the mass in the inflows because the latter entrain some ambient material that is ultimately accreted onto the cloud.

In addition to these flows, small-amplitude turbulent motions were added to the gas, in order to break the symmetry of the setup and allow the development of instabilities in the dense layer formed by the collision (the cloud). As in Paper I, the code was modified to model the formation of sink particles. Specifically, in order to prevent the timestep from becoming arbitrarily small when a certain region of the flow undergoes gravitational collapse, once a region becomes denser than a certain threshold $n_{\rm sf}$, it undergoes a number of tests to determine whether it is collapsing. If the tests are passed, then the mass in the region is removed from the gas phase and a "sink particle" is created, which inherits the total mass and momentum of the removed SPH particles (Bate et al. 1995; Jappsen et al. 2005; Federrath et al. 2010). In turn, the sink particle itself may continue to accrete mass from the gas phase. In the present simulation, we have taken $n_{\rm sf} = 3.2 \times 10^6\,\mathrm{cm}^{-3}$, the same as that in Paper I.[3] In addition, we also implemented the radiative heating and cooling function used in Paper I, which in turn was taken from Koyama & Inutsuka (2002), only correcting some typographical errors. The effect of more realistic cooling functions has been recently investigated by Micic et al. (2013), showing that they are in general minor.

The collision of the flows in the center of the box induces a phase transition in the flow from diffuse-warm to cold-dense gas, producing a dense layer of cold gas that grows in mass over time (Vázquez-Semadeni et al. 2006). The ram pressure-confined dense layer is subject to bending-mode and hydrodynamical instabilities, causing the development of moderately supersonic turbulence within it (Vishniac 1994; Walder & Folini 2000; Heitsch et al. 2005, 2006; Vázquez-Semadeni et al. 2006), which in turn produces nonlinear density fluctuations. Moreover, the dense layer continues to accrete gas from the original inflows, thus increasing its mass. Eventually, as was shown in Paper I, the layer at large becomes gravitationally unstable and begins to contract. Some time later, before the global contraction is completed, the local density fluctuations also become unstable due to the decrease of the average Jeans mass and begin to collapse themselves. Because they are nonlinearly overdense with respect to the global cloud average, they have shorter free-fall times than that of the cloud at large, completing their collapse before the whole cloud does.

[3] Note that in Paper I, there was a typographical error with the threshold density erroneously reported as $10^5\,\mathrm{cm}^{-3}$.

3. GLOBAL EVOLUTION

Paper I aimed at investigating the combined effects of cooling, turbulence generation in the compressed layer (the cloud), and self-gravity, finding that the cloud grows in mass until its gravitational energy overtakes the turbulent kinetic energy, at which time it begins to undergo gravitational collapse. However, the turbulent kinetic energy induced by the instabilities in the compressed layer was not very large (the Mach number was of the order of a few only; see also Vázquez-Semadeni et al. 2010), and velocities corresponding to Mach numbers typical of giant molecular clouds only developed as a consequence of the gravitational collapse, and corresponded to the collapsing motions themselves and not to random turbulence. Several megayears after the onset of global collapse, local collapses began to occur seeded by the density fluctuations produced by the moderately supersonic turbulence produced by the flow collision.

However, in the main simulation of Paper I, of which the present simulation is a remake at higher resolution, most of the early star formation occurred in a high density ring that formed at the circular periphery of the flat cloud caused by the inflowing cylinders. Instead, in the higher-resolution run presented here, the lower numerical viscosity allows the gas to squirt out more freely from the colliding region, so that the high density ring does not form (see Figure 1). This has two implications. First, while in the run from Paper I all the initial local collapses occurred in the peripheral ring, in the present simulation they occur throughout the dense layer. Second, while in Paper I the ring itself quickly began contracting and falling onto the center of the dense layer, here, in the absence of such a ring, both the local and global collapses are less focused, and thus take longer to develop. So, while sink formation started at $t \approx 17$ Myr in Paper I, here it begins at $t \approx 20$ Myr.

Also, the global collapse is less coherent. While in Paper I the time at which the ring reaches the simulation center is very well defined, signaling the culmination of the large-scale collapse, here the dense layer fragments into filaments, which then form clumps, onto which the rest of the filament continues to accrete. This is understood in terms of the fact that the collapse timescale for a long filament of aspect ratio A is longer than that of a roughly spherical clump of the same volume density by a factor between $\sim A^{1/2}$ and $\sim A$, depending on whether the collapse is homologous or proceeds outside-in (Toalá et al. 2012; Pon et al. 2012). Only later, the entire filament-clump system falls into the large-scale potential well at the center of the simulation. Specifically, the free-fall time at the mean initial density of cloud after the phase transition ($\sim 100\,\mathrm{cm}^{-3}$) is ~ 3.3 Myr. However, in practice, the global collapse of the cloud occurs over roughly 20 Myr (see Paper I and Figure 1), from $t \sim 13$ Myr to $t \sim 33$ Myr.

The fact that the usage of higher resolution (and perhaps also the different version of the code) produce a different morphological pattern is a reflection of the chaotic nature of the system, which exhibits sensitivity to initial conditions (i.e., arbitrarily nearby initial conditions end up producing very different states after finite evolution times). However, the

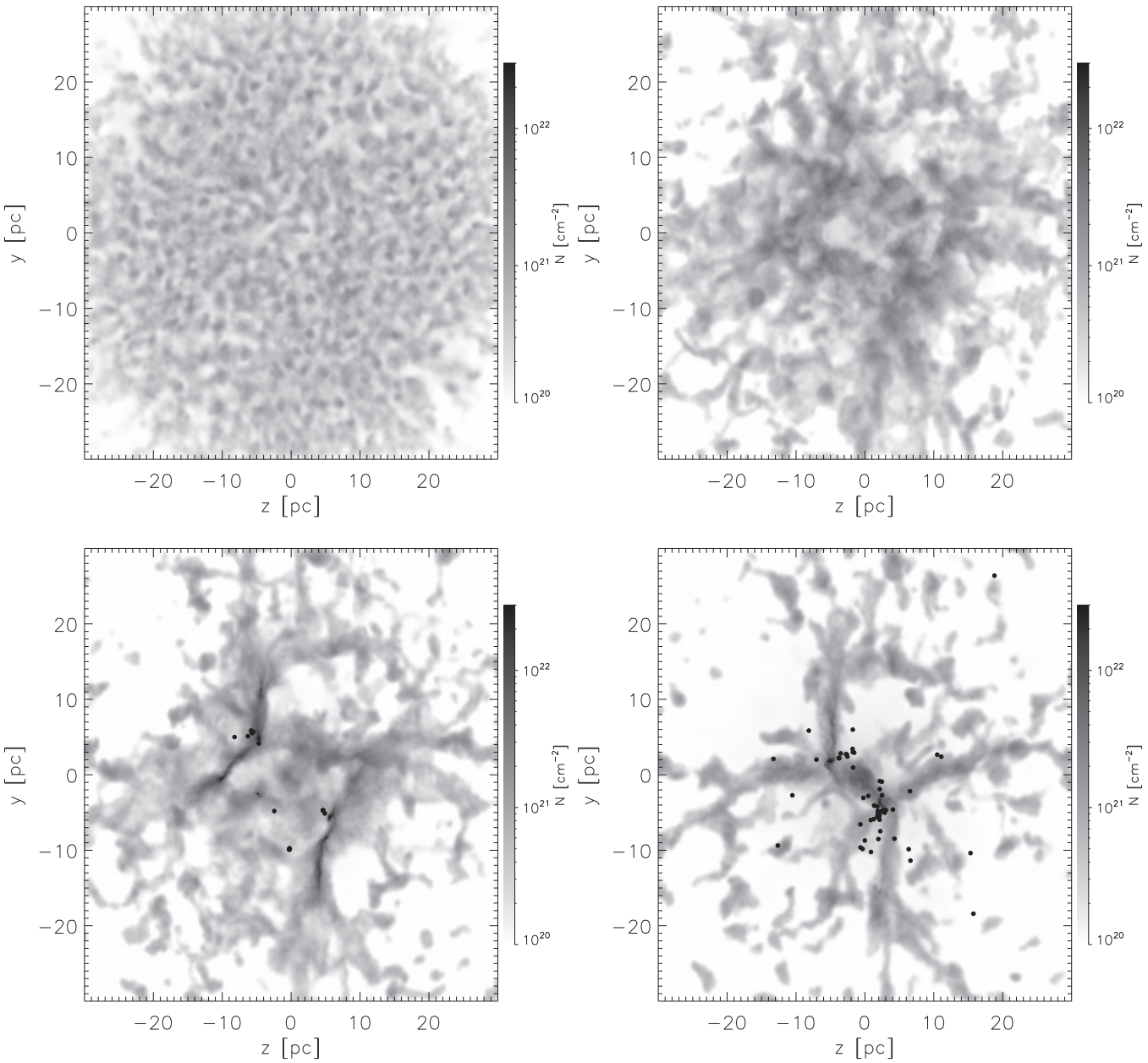

Figure 1. Face-on view of the central 60 pc of the simulation along the axis of the colliding flows. Grayscale represents the gas column density integrated over ±15 pc around the contact point of the initial flows, at the center of the simulation box. Times shown correspond to $t = 9.30$ (top left panel), 17.93 (top right), 23.91 (bottom left), and 30.41 Myr (bottom right) from the onset of the simulation. Dots indicate the positions of the sink particles in the range depicted. Coordinates are measured from the center of the simulation box.

differences occur only at the level of morphological detail, and with timing differences at the ∼15% level. Statistically, the two simulations behave in a similar manner, developing local collapses that culminate earlier than the global collapse.

It is important to remark that the collision of WNM currents, aided by thermal instability, initially forms a planar structure, or sheet-like cloud, which rapidly becomes Jeans-unstable and breaks into filamentary structures. In parallel, the sheet keeps accreting material from the inflows, implying that the amount of gas that has undergone the phase transition into CNM (the cloud's mass) increases in time. In a similar way, once formed, the filaments accrete mass from the larger planar structure, increasing their mass until they become gravitationally unstable; the filaments then collapse as a whole. However, in turn, the filaments fragment into a number of clumps because they have a longer free-fall time than any roughly spherical, Jeans-unstable fluctuation within them (Toalá et al. 2012; Pon et al. 2012). Thus, the clumps within the filaments increase their own density and develop a density contrast with respect to their parent filament. Material from the filament continues to "rain down" (accrete) onto the clumps, while continuing to be fed by the accretion flow from the sheetlike cloud.

The whole system thus constitutes a mass cascade from the largest to the smallest scales in the cloud, similar to that envisioned by Field et al. (2008), except that those authors proposed a process in which the energy released by the collapse at each scale produces random, quasi-isotropic motions at a smaller scale (see their Section 3). Instead, what we observe in our simulation is a continuous gravitational collapse all the way down to the protostar scale, as observed, for example, by Galván-Madrid et al. (2009), Schneider et al. (2010), and Csengeri et al. (2011). Also, a distinctive feature of this cascade is that the

structures at different scales have different morphologies: from sheets to filaments and from filaments to clumps.

A crucial feature of these structures is that *none of them are in equilibrium.* Instead, they represent a continuous flow toward the troughs of the gravitational potential, at both local and global scales, giving rise to a regime of collapses within collapses, or *hierarchical gravitational fragmentation* (Vázquez-Semadeni et al. 2009). Structures are actually *features of the flow* that persist because they continuously being fed by the accretion flow. One very important kind of such features are the filaments, which recently have received much observational attention. In Figure 1, we show four snapshots of the simulation viewed face-on, showing the formation of the filaments and then their merging to form a final dense collapse center. In the remainder of the paper, we now discuss the physical properties of the filaments that develop in our simulation.

It is important to point out that it is difficult to assign a well-defined timescale to the filaments, because typically they last longer than their crossing time, due to the accretion. Moreover, they take time to assemble and to take a well defined shape. In any case, the filaments we discuss in the next section roughly last ∼7 Myr, from $t \sim 21$ to $t \sim 28$ Myr, from the time when they first become discernible to the time when they finish accreting onto their nearest main clump. We choose to study them at a specific time when they appear clearly defined.

4. DENSE FILAMENTS

4.1. Identification

Two major filaments are readily noticeable in the lower left panel of Figure 1 ($t = 17.9$ Myr); we shall refer to the one centered at $(z, y) \approx (-7.6, 2.8)$ pc as "Filament 1," and to the one centered at $(z, y) \approx (6.8, -5.3)$ pc as "Filament 2." Figures 2 and 3 show column density images of Filaments 1 and 2, respectively, in both the (z, y) and the (x, y) planes, 26.56 Myr into the simulation (approximately the midpoint of the times shown in the bottom panels of Figure 1). The coordinates shown in the axes are measured with respect to the center of the simulation box.

When only gas with density $n > 10^3\,\mathrm{cm}^{-3}$ is considered, Filament 1 has a mass ∼560 $M_\odot$ (∼2.4×10^3 $M_\odot$ if we consider gas with $n > 50\,\mathrm{cm}^{-3}$), and is ∼12 pc long and ∼1 pc wide. Its mean density ($5.18 \times 10^4\,\mathrm{cm}^{-3}$, mass-weighted considering gas with $n > 10^3\,\mathrm{cm}^{-3}$ only) and aspect ratio imply an approximate free-fall time of 0.72 Myr (Toalá et al. 2012). Filament 2 has a mass of ∼680 $M_\odot$ when defined by a threshold $n > 10^3\,\mathrm{cm}^{-3}$ (∼2×10^3 $M_\odot$ when gas with $n > 50\,\mathrm{cm}^{-3}$ is considered), has an approximate length of ∼15 pc, and a width ∼1 pc; its mean density ($7.88 \times 10^4\,\mathrm{cm}^{-3}$) and aspect ratio imply an approximate free-fall time of 0.66 Myr.

4.2. Local Gravitational Collapse

As discussed in Section 3, the filaments soon develop dense cores. By the time shown in Figures 2 and 3, some of those collapse centers have already created sink particles (35, totaling 2.24×10^3 $M_\odot$). Thus, each of the individual structures formed from the original collision of WNM currents acts as a channel that funnels mass from the parent to the child structures. Moreover, as time goes on, the scale of the filament-clump system grows, involving increasing amounts of mass and correspondingly larger spatial scales. For example, in the bottom right panel of Figure 1, a large accreting clump is seen to have formed at the center of the frame, with large-scale filaments accreting onto it.

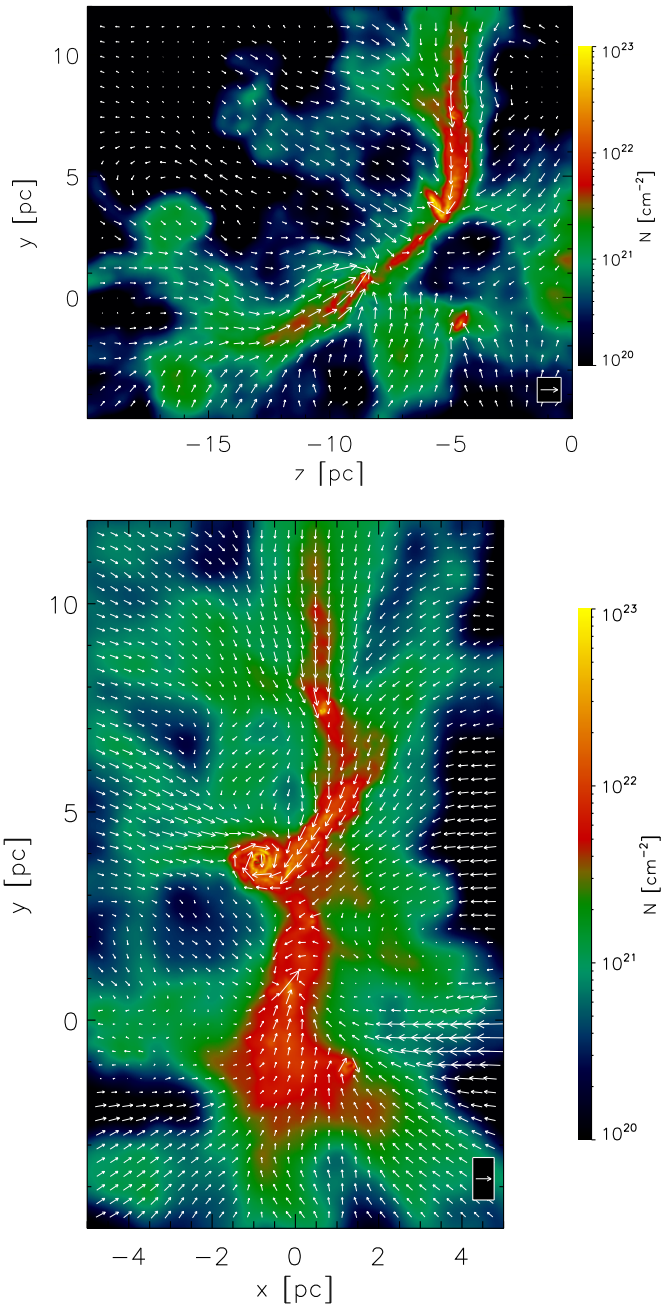

Figure 2. Filament 1 at 26.56 Myr into the simulation. Colors show the column density of the gas integrated over the range $|x| < 5$ pc for the top panel and $-20\,\mathrm{pc} < z < 0$ for the bottom panel. Coordinates are measured with respect to the center of the simulation box. The arrows show the density-weighted projected velocity field with the arrow in the lower right representing 2 km s^{-1}. (A color version of this figure is available in the online journal.)

The picture described above may be verified by exploring the velocity field along the filaments. In order to do this, we have calculated the column density along lines of sight (LOSs) approximately perpendicular to the filaments. We first obtained the density distribution of the gas on two boxes with 512^3 grid points, each containing one of the filaments, with resulting resolution of $(\Delta x, \Delta y, \Delta z) = (0.020, 0.033, 0.039)$ pc for Filament 1, and $(0.020, 0.041, 0.029)$ pc for Filament 2. Then, taking advantage of the fact that the filaments lie on

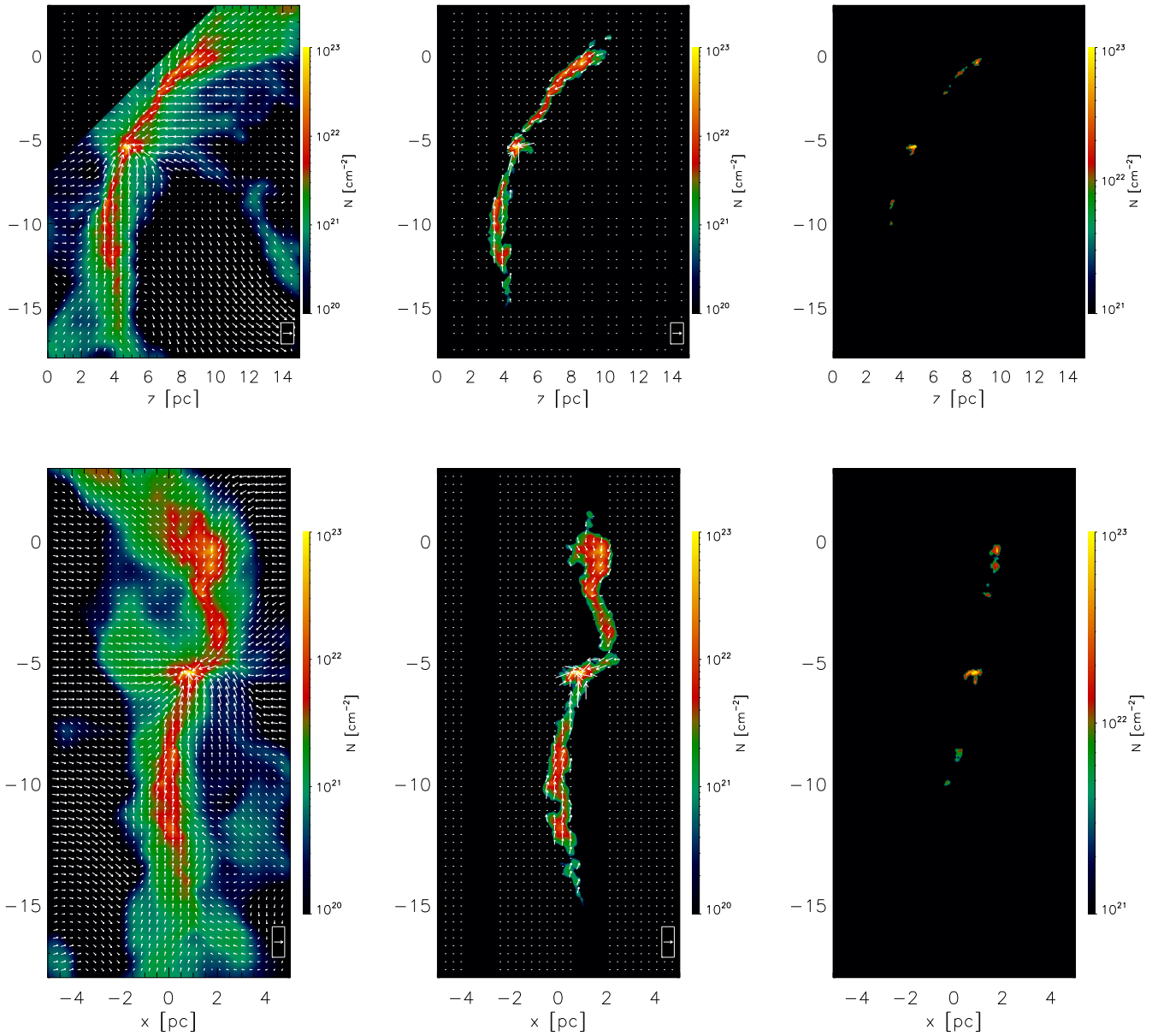

Figure 3. Filament 2 at 26.56 Myr into the simulation, integrated in the ranges $|x| < 5$ pc for the top row, and $0 < z < 15$ pc for the bottom row. The left column shows the total column density, while the middle column shows column density for gas with $n > 10^3$ cm^{-3} and $n > 10^4$ cm^{-3} in the right column. In all cases, the arrows show the density-weighted projected velocity with the arrow in the lower right representing 2 km s^{-1}. The region $z - y \gtrsim 7$ pc is suppressed to avoid a separate condensation unrelated to the filament of interest. The bottom row of this figure is also available as mpeg animations in the online journal.

(Animations and a color version of this figure are available in the online journal.)

the y–z plane, and noting from visual inspection that the LOSs are at angles $\sim -50°$ and $\sim -20°$ from the z axis in Figures 2 and 3, respectively, we thus have rotated the fields by minus these amounts on this plane to orient the filaments vertically.

The resulting column density maps are shown in Figure 4, where the vertical axis, labeled ξ, is now approximately parallel to the filament. Superposed on these maps, we show plots of the column density-weighted mean velocity perpendicular to the LOS and approximately along the filament (the vertical velocity in the projection of Figure 4). This rendering clearly shows the large-scale collapse of the filament along its long dimension, signaled by the sharp transition (jump) from positive velocities in the lower region to negative velocities in the upper region. However, in addition to this global collapse, smaller jumps in velocity associated to smaller-scale (in size and mass) centers of collapse are also observed. The collapsing regions move along the filament, as they follow the large-scale filament collapse, and so the velocity jumps around these regions are superposed on the average infall velocity toward the larger-scale center of mass.

The velocity structure seen in Figure 4 qualitatively resembles that observed in a number of observational studies. In particular, Kirk et al. (2013) report a velocity gradient of 1.4 km s^{-1} pc^{-1} across the filament associated with the embedded Serpens South protocluster (see their Figure 4), while Peretto et al. (2014) report velocity gradients ranging between 0.22 and 0.63 km s^{-1} pc^{-1} across the filaments in SDC13. Although both the size and velocity scales of those filaments are smaller than ours, the velocity difference in our filaments, $\sim$5 km s^{-1} over length scales of $\sim$10 pc, also corresponds to a gradient $\sim$0.5 km s^{-1} pc^{-1}. These results are only preliminary, and a survey of the filaments produced in our simulations should be

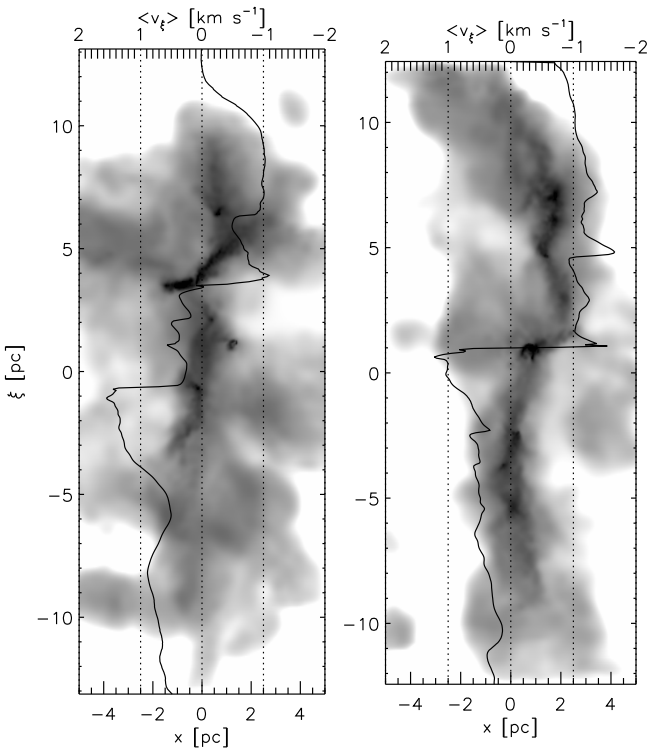

Figure 4. Projections perpendicular to the filaments. The grayscale shows the column density (in the 10^{20} to 3×10^{22} cm^{-2} range, logarithmic scale) along a line of slope $-50°$ in the z–y plane (top panel) of Figure 2 for Filament 1 (left), and $-20°$ in the z–y plane (top panel) of Figure 3 for Filament 2 (right), so that the vertical coordinate here (labeled ξ and measured from the center of mass of each filament) is approximately along the filaments. The solid line shows the column density-weighted ξ velocity, averaged over the filament width. Its value is given by the upper horizontal scale. The global collapse of the filaments, with superimposed local collapses, is apparent.

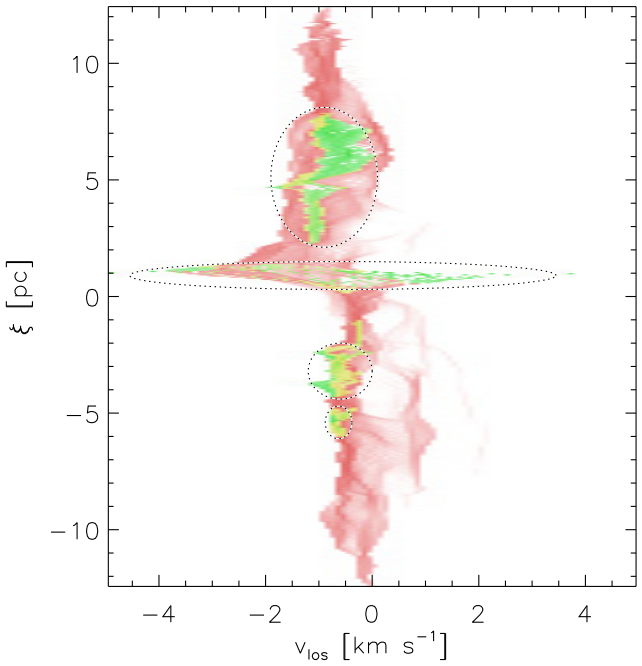

Figure 5. Position–velocity map along the center of the Filament 2, integrated along the same direction as in Figure 4 so that the line of sight is approximately perpendicular to the filament and the ξ coordinate is measured along the filament. The grayscale (red image online) corresponds to gas with $n < 10^3$ cm^{-3}, while contours (green image online) corresponds to denser gas. Both show the column density of gas per unit velocity interval (on a logarithmic scale) in the range $3\times10^{19} - 3\times10^{23}$ cm^{-2}(km s^{-1})$^{-1}$. Denser gas breaks into separate structures, marked with dotted ellipses, while gas at lower density forms a continuous structure along the filament. Most of the gas in both density regimes is clearly separated in velocity space, with only narrow regions of overlap (yellow in the online version).

(A color version of this figure is available in the online journal.)

carried out, but the qualitative similarity between our results and the observations is encouraging.

4.3. Accretion onto and from the Filaments

As mentioned above, the filaments are not depleted in a free-fall time (see Section 4.1) as they fall onto the local collapse centers (the clumps) within them because the filaments themselves are accreting material from their surroundings. This infall of material occurs at lower densities than that of the filaments, and so the infall and the dense filament might not both be observable with the same molecular species. Nevertheless, we report here the accretion structure in the hope that it can be ultimately compared with that of observed filaments.

Figure 5 shows a position–velocity diagram along Filament 2, integrating along the same LOS as in Figure 4, for gas with density both below (grayscale, red in the online version) and above (contours, green in the online version) 10^3 cm^{-3}. The velocity in this case is along the LOS, and denoted $v_{\rm los}$. While gas with $n < 10^3$ cm^{-3} forms a continuous structure along the filament, gas with $n > 10^3$ cm^{-3} breaks into four separate structures, enclosed by dotted ellipses in Figure 5. One of those individual structures is a disk surrounding a collapse region near the center of the filament (at $\xi \approx 0.5$ pc), distinguishable by the larger spread in LOS velocity. Smaller collapse centers are also noticeable (at $\xi \approx -5.5$, -3, and 5 pc). Interestingly, LOS velocity jumps are generally observed in both the local and the large-scale clump-filament systems

As shown in Figure 3, the gas falls onto the filament in an oblique direction, and gradually becomes a flow *along* the filament as one moves toward the filament's axis. That is, this change of direction happens as the gas density increases. Therefore, when considering the velocity component perpendicular to the filament ($v_{\rm los}$ in Figure 5), gas in different density regimes should separate in velocity space. This is noticeable in Figure 5 as a clear separation of the gas in these regimes (red and green images in the online version), with only a small superposition (visible as a yellow area in the online version), with exception of the disk near the center, where the nature of the gas flow is different from the rest of the filament.

The structure seen in Figure 5 is remarkably similar to that observed by Schneider et al. (2010) in molecular line emission from the DR21 massive filament in the Cygnus X region, which has a length ∼15 pc, very similar to that of the filaments we analyze. Schneider et al. (2010) conclude that the kinematics of the gas is consistent with a global gravitational collapse and inflow onto the filament, in agreement with the dynamical state of our filaments. Furthermore, they show, in their Figure 6, a position–velocity diagram for several molecular transitions that closely resembles our Figure 5. In particular, a separation of different density regimes in velocity space, which in our simulation corresponds to gas falling onto the filament, is observed in their Figure 6. Moreover, the structure in their filament also exhibits significant widenings in the velocity coordinate, of amplitude several km s^{-1}, at the location of clumps. In our simulation, these widenings are the result of the large infall velocities that develop in the vicinity of the clumps.

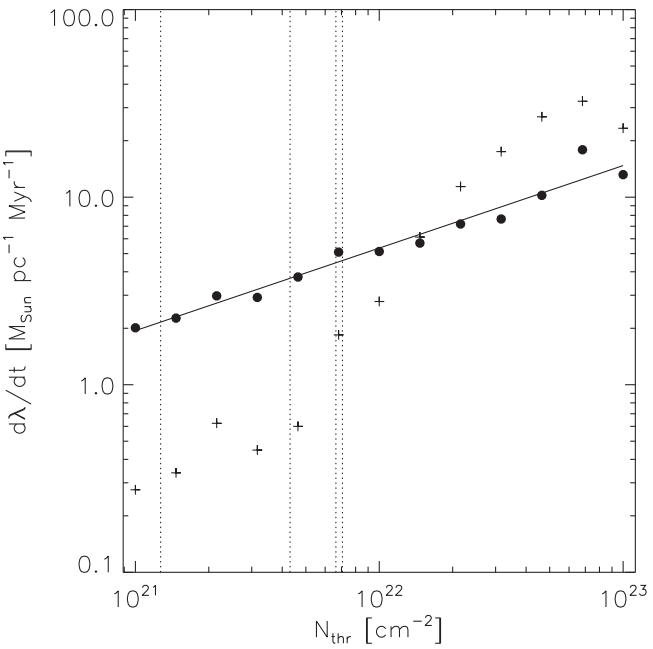

Figure 6. Accretion rate onto Filament 2, defined as the mass flux across the contour containing the column density $N_{\rm thr}$ in the directions perpendicular (dots) and parallel (crosses) to the filament. Dotted vertical lines show column densities corresponding to radii 0.03, 0.1, 0.3, and 1 pc (right to left), according to the fit to the column density profile discussed in Section 4.4. At $N > 10^{22}\,{\rm cm}^{-2}$, the filament's radius cannot be derived from the column density profile fit. The structures at column densities larger than these are isolated clumps, rather than part of the fitted filament radial column density profile. The perpendicular accretion may be fitted by $d\lambda/dt = 5.35\,M_\odot\,{\rm pc}^{-1}\,{\rm Myr}^{-1}(N/10^{22}\,{\rm cm}^{-2})^{0.44}$ (solid line).

These similarities strongly suggest that the filament studied by Schneider et al. (2010) is indeed produced, like the filaments in our simulation, by gravitational collapse.

Figure 6 shows the projected accretion rate onto Filament 2, defined as the flux across a contour defined by a given column density value (integrated along the LOS approximately perpendicular to the filament described above). Shown are both the flux across longitudinal contour segments (the flux perpendicular to the filament; filled circles) and across a contour segment perpendicular to the filament (the flux along the filament; plus signs). As mentioned above, the filament accretes gas mainly in the direction perpendicular to it. However, since the filament itself is falling onto the clump at the same time it is accreting, the inflow parallel to the filament, although small, is non-negligible. For example, at a threshold density of $3 \times 10^{21}\,{\rm cm}^{-2}$, the flux along the filament is a factor of $\sim$10 smaller than the perpendicular accretion. In the scenario pictured above, this should not be surprising: the filament flows along its long direction, but keeps being replenished by its envelope. So, at a surface defined solely by a column density value there will be flux due to both accretion (mainly perpendicular) onto the filament as well as flux (parallel) corresponding to infall due to the collapse of the filament as a whole.

The accretion rate along the filament becomes comparable to the perpendicular one at $N_{\rm thr} \sim 2 \times 10^{22}\,{\rm cm}^{-2}$. This may be understood in terms of mass conservation, since the filament is not a hydrostatic structure, but rather, a flow feature, so that all the mass that accretes perpendicularly to the filament must eventually flow away in the longitudinal direction. Considering that the filament is $\sim$15 pc long, its total perpendicular accretion rate is $\sim$150 $M_\odot\,{\rm Myr}^{-1}$.

4.4. Filament Profile

4.4.1. Column Density Fit

It has been suggested that filaments observed in molecular clouds might have a Plummer-like profile in the direction perpendicular to the filament's long axis. Arzoumanian et al. (2011) explored a number of filaments observed with *Herschel* and fitted a profile with a core of constant density ρ_c and radius R_c, and a power-law envelope of the form

$$\rho_P(R) = \frac{\rho_c}{[1+(R/R_c)^2]^{p/2}}, \quad (1)$$

where R is the distance perpendicular to the filament's long axis and p is the (negative) logarithmic slope of the density profile at large R. The corresponding column density perpendicular to the filament is (Arzoumanian et al. 2011)

$$\Sigma_P(R) = \frac{A_p \rho_c R_c}{[1+(R/R_c)^2]^{(p-1)/2}}, \quad (2)$$

where $A_p = \int_{-\infty}^{\infty} du/(1+u^2)^{p/2}$. They found that the filaments are well fitted for values of p in the range $1.5 < p < 2.5$, and a characteristic Gaussian FWHM of 0.1 pc, which corresponds to $R_c \approx 0.03$ pc.

We wish to compare the filaments in our simulation with the results of Arzoumanian et al. (2011). However, this is not completely straightforward, as the column density structure around the filaments is far from being smooth, being instead significantly clumpy. Also, the radial column density profile is in general asymmetric around the maximum. For example, in the lower left panel of Figure 3, a moderate-density clump is observed at $(x, y) \approx (3, -12)$ pc, which extends $\sim$3 pc in the y direction while a protrusion is observed coming off the filament at $(x, y) \approx (-1, -5)$ pc. If a single Plummer-like profile were to be fitted to the spatial column density distribution, these neighboring clumps would induce strong local variations in the fitted parameters of the column density profile, namely, the position of the density maximum (the "spine" of the filament), the central density ρ_c, the width R_c, and the slope p).

In order to minimize the impact of the irregularities, we have chosen to use a two-step fitting procedure, as follows. First, in order to best locate the axis of the filament, we fit a composite profile consisting of *the sum* of two Plummer-like components, each of the forms of Equation (2), to the column density at each position ξ along the filament where the peak column density exceeds $2 \times 10^{21}\,{\rm cm}^{-2}$. The fit is performed using a χ^2 minimization technique. This procedure then gives us two sets of parameters, one for each component. Figure 7 illustrates this procedure.

In the second step, we then assume that the "true" position of the filament's spine is the one given by the fitted component with the higher central column density. We then drop all other information from the two-component fit, and perform a new, single-component fit to the *mean* radial column density profile, with the averaging performed over both sides of this central position and along the filament's length.

Figure 8 shows the resulting mean profile. The best fit to this mean profile has $R_c = 0.31$ pc, $\rho_c/m_{\rm eff} = 3.0 \times 10^3\,{\rm cm}^{-3}$, and $p = 2.4$. This filament width is consistent with the filament data compiled by Myers (2009) for a number of nearby star-forming regions. We also added a constant column density term to the model in order to account for the low density diffuse gas present in the simulation that is not observable in molecular line

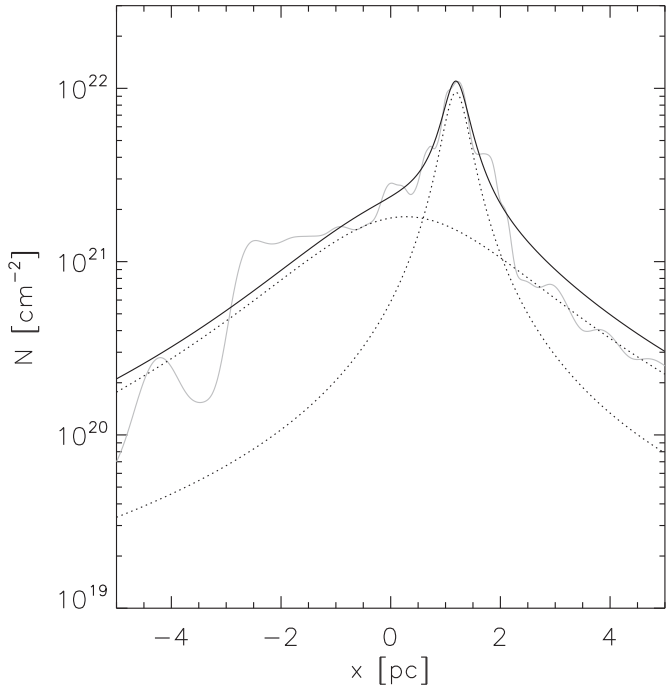

Figure 7. Example of how the two-Plummer-components fit is performed for a given radial density or column density profile. The fitted function is the sum of two Plummer profiles, each with a different set of parameters, so that one of them captures the position of the actual maximum, while the other allows for an asymmetry of the physical profile. The dotted lines show the two fitted components, while the dark solid line shows the total fitted profile, and the gray solid line shows the actual column density profile corresponding to the Filament 2 at $\xi = 1.22$ pc (see Figure 4).

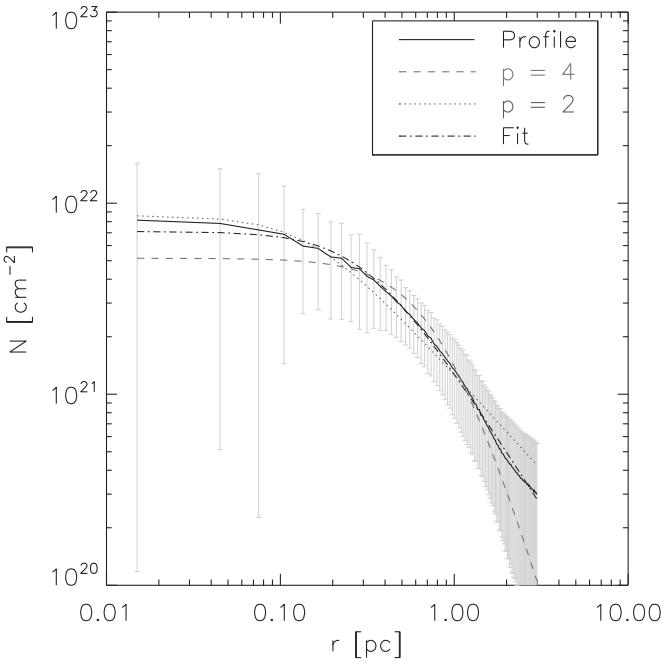

Figure 8. Mean column density profile for Filament 2 (solid line) as a function of distance perpendicular to the filament. Error bars show the spread of column density profiles for different values of ξ. The best fit of the form of Equation (2) (dot-dashed line) is shown, along with fits with $p = 2$ and 4 (dotted and dashed lines, respectively) for comparison.

emission, but the resulting column density base is negligible (3.8×10^{17} cm^{-2}) and the fitted profile parameters change only marginally. In both cases, the spread in column density profiles along the filament is much larger than the error in the fit.

Figure 8 also shows the fitted profile for the $p = 4$ case, which corresponds to an isothermal cylinder in hydrostatic equilibrium (Ostriker 1964). With the appropriate parameters, a $p = 4$ model can be fitted within the large spread in column density values. However, departures from the average profile show trends (systematically below the mean profile in the constant core region, for example), suggesting a bad fit. Also, since the $p = 4$ model falls more rapidly than the mean profile, the fit is more sensitive to the constant column density term mentioned above (in fact, this is the only case where a non-negligible column density base was returned by the fitting procedure, namely, 3×10^{20} cm^{-2}). Regardless, a bad fit for a hydrostatic model should not be surprising given the dynamical nature of the filament in the simulation. In fact, Figure 8 also shows a fit with $p = 2$, which Arzoumanian et al. (2011) used to fit one of their filaments. It is seen that this value of p provides a much better fit for our filament than the case $p = 4$, although the best fit is obtained for $p = 2.4$.

Fitting a column density profile of the form of Equation (2) to Filament 1 is less reliable than in the case of Filament 2 since Filament 1 bends and has more nearby small-scale concentrations that skew the fit. Nevertheless, considering only the gas below the disk ($\xi \leqslant 3.5$ pc) and masking out the concentration at $(x, \xi) \approx (1, 1)$ pc (see left panel in Figure 4), the fitting procedure yielded similar central density and core radius values ($\rho_c/m_{\rm eff} = 1.8 \times 10^3$ cm^{-3} and $R_c = 0.29$ pc), although with a shallower profile ($p = 2.0$).

4.4.2. Volume Density Fit

In contrast with observations, the numerical model yields the full spatial distribution of the gas, allowing us to explore the three-dimensional structure of the filament. With this in mind, we repeated the above procedure but using a profile of the form of Equation (1) to fit the volume density distribution of the Filament 2. In this case, the two-step fit was performed at each ξ position along the filament, this time considering the density field in a plane perpendicular to the ξ coordinate. The fit was only performed if the maximum density on this plane, $n_{\rm max}$, satisfied $n_{\rm max} > 10^3$ cm^{-3}. Again, the main component is defined as that with larger central column density (the product $\rho_c R_c$).

Figure 9 shows the fitted parameters along the filament. The fitting procedure returns continuous positions for the center of the main component along the filament, suggesting that it is reasonably well defined by the fit. However, it is noteworthy that the distribution of centers of the secondary component, although not really continuous, tends to agglomerate to the right of the main component. This behavior is also present in the distribution of ρ_c and p values along the filament. We envision two possible interpretations. One is that the filament is really a bundle of smaller filaments, as proposed by Hacar et al. (2013) for filaments in the Taurus region, that may be separated in velocity space. Another interpretation, which we find more plausible, is that the filament is not symmetric and so, using a symmetric form for the fit (either in real or in velocity space), artificially yields multiple, displaced components. This lack of symmetry is suggested by the skewed velocities in Figure 5.

With the center of the filament defined by the main component, we may average to obtain a (cylindrically symmetric) density and velocity profiles characteristic of the filament. Such profiles are shown in Figure 10. As the gas is accreted into the filament, the radially inflowing velocity changes direction,

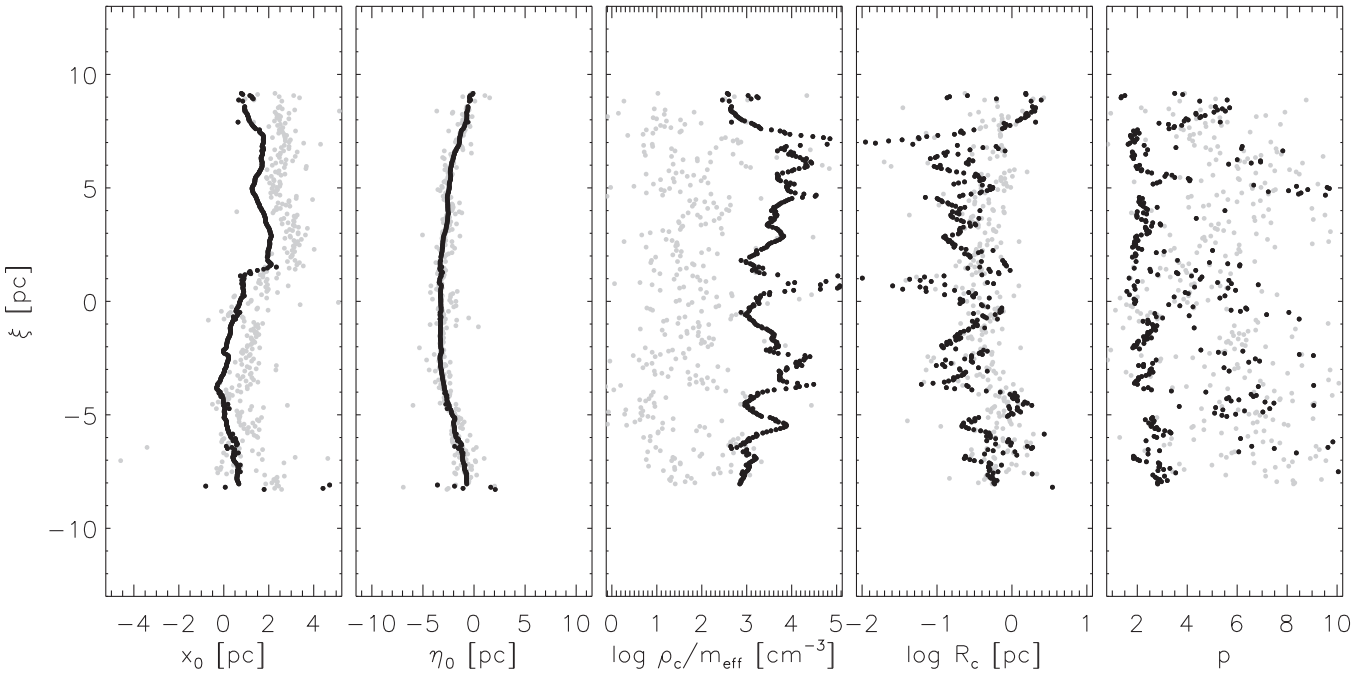

Figure 9. Resulting parameters when a two-component profile of the form of Equation (1) is fitted to Filament 2. The parameters x_0 and η_0 represent the coordinates of the center of the profile, with η being the direction along the line of sight (perpendicular to the plane of the figure) in Figure 4. Dark dots correspond to the main component of the fit, while light dots show the secondary component. The parameters for the secondary component are seen to fluctuate strongly, reflecting the random nature of the clumps in the vicinity of the main filament.

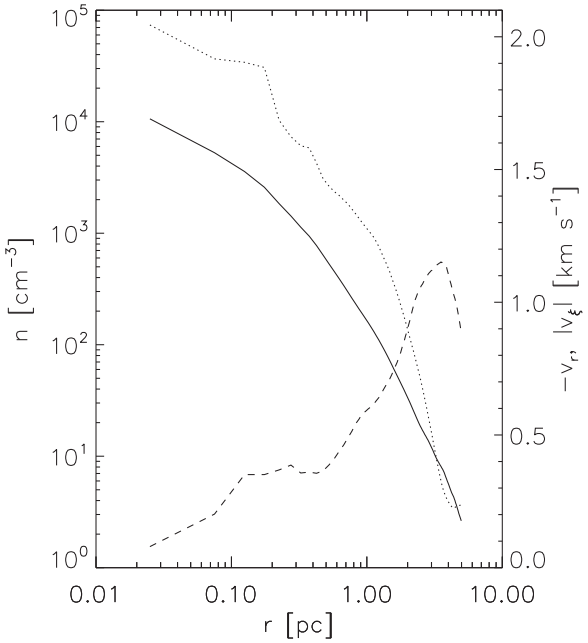

Figure 10. Azimuthally averaged density (solid line), radial infall velocity (dashed), and longitudinal velocity (dotted) for Filament 2. As gas is accreted onto the filament, its (radial) inflowing velocity gradually changes direction, so that the gas in the centermost regions flows mainly along the filament.

turning the gas motion into a flow along the filament. It does not appear to happen abruptly (through a shock, for example), but in a smooth way. This change in the flow direction is apparent also in Figures 2 and 3.

Following Arzoumanian et al. (2011), the averaged radial density profile was then fitted by a single Plummer-like shape. In this case, the best single-component fit has parameters $R_c = 0.11\,\mathrm{pc}$, $\rho_c/m_{\rm eff} = 8.6 \times 10^3\,\mathrm{cm}^{-3}$, and $p = 1.9$. This value of p implies a shallower volume density profile than the corresponding column density one. This is, however, to be expected, as the column density, seen in projection, increases toward the central axis of the filament due to the combined effects of a larger volume density at the central axis and of a longer integration path there. Nevertheless, without the smoothing effect provided by the LOS integration, the spread in values in the volume density profiles is much larger than in the column density case. This sends a warning that the actual three-dimensional structure of observed filaments may be significantly more disordered and chaotic than what might be inferred from fits to the column density, which constitutes a LOS average, and are furthermore averaged along the length of the filament.

5. LIMITATIONS AND RESOLUTION CONSIDERATIONS

Our analysis is not free of caveats and limitations. First, we only analyzed two filaments, as a proof-of-concept, and only at a single typical scale, although filaments at different size and mass scales are apparent in the simulation. In the future, we plan to perform a systematic survey-like study, applying an automated filament-detection algorithm, which should allow us to obtain significant statistics and investigate scaling properties.

Second, our simulations have omitted a number of physical processes, most notably magnetic fields and stellar feedback. In particular, the omission of stellar feedback implies that our study should be applicable only to the early evolutionary stages of the filament-clump system. On the other hand, magnetic fields have been suggested to have an important role in the formation and structuring of filaments (e.g., Padoan et al. 2001; Hennebelle & André 2013), so a study analogous to the one we have presented here should be performed including magnetic fields. Nevertheless, the fact that our filaments compare reasonably well with observations suggests that the magnetic field may only play a relatively minor role.

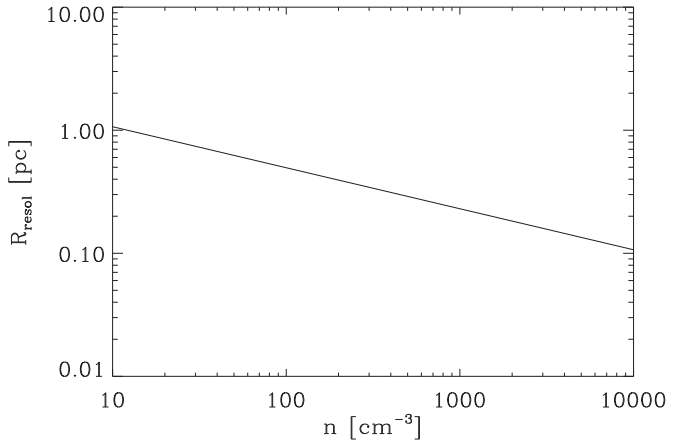

Figure 11. Minimum resolved size scale as a function of density, computed as the radius of a sphere at the indicated density, and containing twice the mass within the smoothing length of the code (i.e., the mass of 80 SPH particles, corresponding to $m = 1.6\,M_\odot$).

Third, it is important to estimate the level at which our filamentary structures are resolved. This can be done as follows. A standard resolution criterion with SPH is that the minimally resolved mass is twice that contained within a smoothing length. Our simulation employed 40 neighbors to define the smoothing length. Given the SPH particle mass of $\approx 0.02\,M_\odot$ (see Section 2), the minimally resolved mass is $m \approx 1.6\,M_\odot$. To determine a corresponding size scale at a given density, we consider the radius of a sphere containing this mass at the specified density, given by $R_{\rm resol} = (3m/4\pi\rho)^{1/3}$. Figure 11 shows the scaling of $R_{\rm resol}$ with density. This can be compared with the size scales determined for our filaments in Section 4.4. There, we found that the *column* density profiles were well fitted by $R_c \approx 0.3$ pc and $\rho_c/m_{\rm eff} \sim 2$–$3 \times 10^3\,{\rm cm}^{-3}$. By comparison, we see from Figure 11 that, at $n = 2.5 \times 10^3\,{\rm cm}^{-3}$, $R_{\rm resol} \approx 0.17$ pc, so that the fitted central scale is roughly twice the minimum resolved scale, and we can consider that this fit is safely resolved.

On the other hand, also in Section 2, we found that the *volume* density profile was fitted with $R_c \approx 0.11$ pc and $\rho_c/m_{\rm eff} \approx 8.6 \times 10^3\,{\rm cm}^{-3}$. For comparison, we see from Figure 11 that at $n = 8.6 \times 10^3\,{\rm cm}^{-3}$, $R_{\rm resol} \approx 0.11$ pc, so in this case the fit is only marginally resolved. Thus, we cannot rule out the possibility that the characteristic width of our filaments may be limited by resolution.

Nevertheless, despite the relative simplicity and resolution limitations of the simulations presented here, the fact that a simulation originally designed to study a different phenomenon (the evolution of the star formation activity before feedback dominates) yields filaments similar to observed ones suggests that the dominant physical processes involved in the filament dynamics are present in the simulation.

6. SUMMARY AND CONCLUSIONS

We performed SPH simulations of the formation of a molecular cloud from a convergent flow of diffuse gas. As in previous works, the resulting cloud is highly dynamic and, due to hydrodynamic and thermal instabilities, becomes turbulent and rapidly fragments into substructure. Nevertheless, the "turbulent" motions are unable to stabilize the cloud and soon its dynamics becomes dominated by gravity and the cloud begins to collapse. However, because the cloud continues to accrete, its mass continues to grow, and soon it contains a large number of Jeans masses (Vázquez-Semadeni et al. 2007). This naturally leads to the formation of filaments, since the multi-Jeans mass flow behaves similarly to a pressureless flow, which is known to collapse along its shortest dimension first (Lin et al. 1965), so that the initially planar cloud collapses onto filaments, which then collapse into clumps.

The filaments are not equilibrium structures at all, and instead are highly dynamical. They can be considered intermediate steps of the cloud's collapse, constituting channels through which the gas is funneled from the extended cloud onto the clumps. These filaments are the loci of colliding streams on the parent planar structures, where the flow gets reoriented and directed toward its final destination—the clumps within the filaments, which have conditions appropriate for star formation.

It is important to remark that the filaments developing in our simulation arise self-consistently from the fragmentation of the cloud initially formed by the convergence of warm gas streams by the combined action of various instabilities (Heitsch et al. 2005). In particular, thermal instability produces small, cold clumps that grow by the accretion of warm gas as well as by merging with other clumps (Banerjee et al. 2009) until they finally become gravitationally unstable and begin to collapse. Thus, our simulation differs fundamentally from simulations of *Fourier-generated* turbulence in the multi-phase medium, in which the external velocity field is constructed in Fourier space and is applied everywhere in space (e.g., Vázquez-Semadeni et al. 2000, 2003b; Gazol et al. 2005, 2009; Goodwin et al. 2004, 2006; Gazol & Kim 2010, 2013; Bate 2009; Walch et al. 2012). The latter method allows precise control of the driving scale, the amplitude, and nature (ratio of solenoidal to compressible energy) of the applied force, albeit at the expense that the driving is applied as a body force rather than as a surface stress, as corresponds to the kind of energy sources present in the ISM, such as outflows and expanding shells. Instead, in our simulation, the characteristic (or "energy-containing") scale of the turbulence, as well as the amplitude and ratio of solenoidal to compressible, develop self-consistently from the instabilities in the compressed layer and we have no control over these parameters.

Under these conditions, in our simulation, the gravitational collapse in the individual centers (modeled with sink particles), is not instantaneous but starts $\sim$20 Myr into the simulation and continues well after the filaments finish to accrete onto the clumps. Moreover, the filaments themselves are falling into the largest-scale potential well, generating new structures that eventually merge into each other, forming a larger-scale hub-filament system toward the end of the simulation.

The simulation presented here formed two prominent filaments, each with $\sim 600\,M_\odot$ out to radii $\sim$0.3 pc and lengths of $\sim$15 pc, implying linear mass densities $\lambda \sim 40\,M_\odot\,{\rm pc}^{-1}$. We furthermore studied the radial density and column density profiles of such filaments, finding that the column density profile is reasonably well fitted by a Plummer-like profile whose best-fit parameters are $R_c = 0.31$ pc and $p = 2.4$. In turn, the three-dimensional radial density distribution was best fitted with $R_c = 0.1$ pc and $p \approx 1.9$, although this fit was less certain because in the three-dimensional measurement no averaging along the LOS is made.

These values are qualitatively consistent with observational results. For example, André et al. (2010) find that their sample of filaments in the Aquila region have linear mass densities

$\lambda > 15\,M_\odot\,\mathrm{pc}^{-1}$, while Arzoumanian et al. (2011) find that their filaments typically have Plummer-type column density radial profiles with $R_c \sim 0.1$ pc and $1.5 < p < 2.5$. These authors speculate that their filaments may form as the result of the dissipation of large-scale turbulence, because their characteristic thickness is similar to that of the sonic scale, below which the "turbulence" becomes subsonic. However, in our case, the filaments are not a result of turbulence and their thickness is not the result of having dissipated the turbulence. Instead, they are an intermediate stage of the gravitational collapse, funneling gas to the local collapse centers—the clumps—and their thickness appears to be the result of the force balance between the radial pressure gradient in the filament and the combined thermal plus ram pressure of the gas falling onto the filament, the whole system maintained in a stationary state thanks to the "drainage" and reorientation of the infalling material toward the trough of the gravitational potential well, located at the clumps accreting from the filaments. We plan to will explore this scenario in a future study.

We also measured the accretion rates perpendicular (onto) and parallel (along) the filament. The rates are not unique, but instead depend on the radial position along the filament. Because of the column density profile, this translates into a column density dependence of the accretion rates. We found that as the column density varies from 10^{21} to $10^{23}\,\mathrm{cm}^{-2}$, the accretion rate per unit length perpendicular to the filament (i.e., onto it) ranges between 2 and 20 $M_\odot\,\mathrm{Myr}^{-1}\,\mathrm{pc}^{-1}$, while the linear accretion density from the filament onto the clump ranges between 0.3 and 30 $M_\odot\,\mathrm{Myr}^{-1}\,\mathrm{pc}^{-1}$. Considering that the filament is $\sim$15 pc long, its total perpendicular accretion rate is $\sim 150\,M_\odot\,\mathrm{Myr}^{-1}$.

Our measured accretion rates, which peak at $2\text{–}3 \times 10\,M_\odot\,\mathrm{pc}^{-1}\,\mathrm{Myr}^{-1}$, are at least half an order of magnitude lower than those inferred by Schisano et al. (2014), although their estimate was an indirect one, assuming that the characteristic timescale for the process of moving the material along the filament is equal to that of the lifetime of the protostellar objects being formed in the clumps, $\sim 10^4$ yr. This is a rather uncertain assumption, which may overestimate the accretion rate estimate. On the other hand, our total measured accretion rate of $\sim 150\,M_\odot\,\mathrm{Myr}^{-1}$ matches very well that inferred by Kirk et al. (2013) ($\sim 130\,M_\odot\,\mathrm{Myr}^{-1}$). However, the filament they studied was at a much smaller (sub-pc) scale, and therefore the comparison may not be conclusive.

We conclude from our results that the process of hierarchical (i.e., multi-scale) and chaotic (i.e., disordered) gravitational fragmentation produces filaments that have physical conditions and accretion rates which are qualitatively similar to those found in recent observational studies, suggesting that this mechanism may indeed be responsible for their formation. However, more systematic studies need to be performed where the mass and size scales of the filaments in both the observations and simulations are better matched, in order to determine whether in this case their radial column density profiles and accretion rates match at the quantitative level. We plan to perform such a study in the near future.

We thankfully acknowledge N. Schneider for useful comments on this work, and two anonymous referees whose reports helped in significantly improving the clarity of the paper. This work has received financial support from UNAM-DGAPA PAPIIT grant IN111313 to G.C.G. and CONACYT grant 102488 to E.V.S. The numerical simulation was performed on the cluster at our Center acquired through the latter grant.

REFERENCES

André, P., Men'shchikov, A., Bontemps, S., et al. 2010, A&A, 518, L102
Arzoumanian, D., André, P., Didelon, P., et al. 2011, A&A, 529, L6
Audit, E., & Hennebelle, P. 2005, A&A, 433, 1
Bally, J., Lanber, W. D., Stark, A. A., & Wilson, R. W. 1987, ApJL, 312, L45
Balsara, D., Ward-Thompson, D., & Crutcher, R. M. 2001, MNRAS, 327, 715
Banerjee, R., Vázquez-Semadeni, E., Hennebelle, P., & Klessen, R. S. 2009, MNRAS, 398, 1082
Bate, M. R. 2009, MNRAS, 397, 232
Bate, M. R., Bonnell, I. A., & Price, N. M. 1995, MNRAS, 277, 362
Battersby, C., Ginsburg, A., Bally, J., et al. 2014, ApJ, 787, 113
Bond, J. R., Kofman, L., & Pogosyan, D. 1996, Natur, 380, 603
Burkert, A., & Hartmann, L. 2004, ApJ, 616, 288
Cantalupo, S., Arrigoni-Battaia, F., Prochaska, J. X., Hennawi, J. F., & Madau, P. 2014, Natur, 506, 63
Carroll-Nellenback, J., Frank, A., & Heitsch, F. 2014, ApJ, 790, 37
Clark, P. C., & Bonnell, I. A. 2005, MNRAS, 361, 2
Colín, P., Vázquez-Semadeni, E., & Gómez, G. C. 2013, MNRAS, 435, 1701
Csengeri, T., Bontemps, S., Schneider, N., Motte, F., & Dib, S. 2011, A&A, 527, A135
Curry, C. L. 2000, ApJ, 541, 831
de Avillez, M. A., & Breitschwerdt, D. 2004, A&A, 425, 899
Dickey, J. M., Salpeter, E. E., & Terzian, Y. 1977, ApJL, 211, L77
Dobbs, C. L., Burkert, A., & Pringle, J. E. 2011, MNRAS, 413, 2935
Elmegreen, B. G. 1987, ApJ, 312, 626
Federrath, C., Banerjee, R., Clark, P. C., & Klessen, R. S. 2010, ApJ, 713, 269
Federrath, C., & Klessen, R. S. 2012, ApJ, 761, 156
Federrath, C., & Klessen, R. S. 2013, ApJ, 763, 51
Feitzinger, J. V., Perschke, M., Haynes, R. F., Klein, U., & Wielebinski, R. 1987, VA, 30, 243
Field, G. B., Blackman, E. G., & Keto, E. R. 2008, MNRAS, 385, 181
Field, G. B., Goldsmith, D. W., & Habing, H. J. 1969, ApJL, 155, L149
Galván-Madrid, R., Keto, E., Zhang, Q., et al. 2009, ApJ, 706, 1036
Gazol, A., & Kim, J. 2010, ApJ, 723, 482
Gazol, A., & Kim, J. 2013, ApJ, 765, 49
Gazol, A., Luis, L., & Kim, J. 2009, ApJ, 693, 656
Gazol, A., Vázquez-Semadeni, E., & Kim, J. 2005, ApJ, 630, 911
Gazol, A., Vázquez-Semadeni, E., Sánchez-Salcedo, F. J., & Scalo, J. 2001, ApJL, 557, L121
Gehman, C. S., Adams, F. C., & Watkins, R. 1996, ApJ, 472, 673
Goldsmith, P. F., Heyer, M., Narayanan, G., et al. 2008, ApJ, 680, 428
Gómez, G. C., Vázquez-Semadeni, E., Shadmehri, M., & Ballesteros-Paredes, J. 2007, ApJ, 669, 1042
Goodwin, S. P., Whitworth, A. P., & Ward-Thompson, D. 2004, A&A, 423, 169
Goodwin, S. P., Whitworth, A. P., & Ward-Thompson, D. 2006, A&A, 452, 487
Gutermuth, R. A., Bourke, T. L., Allen, L. E., et al. 2008, ApJL, 673, L151
Hacar, A., Tafalla, M., Kauffmann, J., & Kovács, A. 2013, A&A, 554, 55
Hartmann, L., & Burkert, A. 2007, ApJ, 654, 988
Heiles, C., & Troland, T. H. 2003, ApJ, 586, 1067
Heitsch, F., Ballesteros-Paredes, J., & Hartmann, L. 2009, ApJ, 704, 1735
Heitsch, F., Burkert, A., Hartmann, L. W., Slyz, A. D., & Devriendt, J. E. G. 2005, ApJL, 633, L113
Heitsch, F., & Hartmann, L. 2008, ApJ, 689, 290
Heitsch, F., Hartmann, L. W., Slyz, A. D., Devriendt, J. E. G., & Burkert, A. 2008, ApJ, 674, 316
Heitsch, F., Slyz, A. D., Devriendt, J. E. G., Hartmann, L. W., & Burkert, A. 2006, ApJ, 648, 1052
Hennebelle, P., & André, P. 2013, A&A, 560, A68
Hennebelle, P., & Chabrier, G. 2011, ApJL, 743, L29
Hennebelle, P., & Pérault, M. 1999, A&A, 351, 309
Henning, T., Linz, H., Krause, O., et al. 2010, A&A, 518, L95
Hoyle, F. 1953, ApJ, 118, 513
Hunter, J. H., Jr., Sandford, M. T., II, Whitaker, R. W., & Klein, R. I. 1986, ApJ, 305, 309
Jappsen, A.-K., Klessen, R. S., Larson, R. B., Li, Y., & Mac Low, M.-M. 2005, A&A, 435, 611
Jenkins, E. B., & Tripp, T. M. 2011, ApJ, 734, 65
Juvela, M., Pelkonen, V.-M., & Porceddu, S. 2009, A&A, 505, 663
Kalberla, P. M. W., Schwarz, U. J., & Goss, W. M. 1985, A&A, 144, 27
Kim, W.-T., Ostriker, E. C., & Stone, J. M. 2002, ApJ, 581, 1080
Kirk, H., Myers, P. C., Bourke, T. L., et al. 2013, ApJ, 766, 115
Klein, R. I., & Woods, D. T. 1998, ApJ, 497, 777
Klessen, R. S., Heitsch, F., & Mac Low, M.-M. 2000, ApJ, 535, 887
Klessen, R. S., & Hennebelle, P. 2010, A&A, 520, A17
Koyama, H., & Inutsuka, S.-I. 2000, ApJ, 532, 980
Koyama, H., & Inutsuka, S.-i. 2002, ApJL, 564, L97

Kritsuk, A. G., Norman, M. L., Padoan, P., & Wagner, R. 2007, ApJ, 665, 416
Krumholz, M. R., & McKee, C. F. 2005, ApJ, 630, 250
Larson, R. B. 1985, MNRAS, 214, 379
Lin, C. C., Mestel, L., & Shu, F. H. 1965, ApJ, 142, 1431
McKee, C. F., & Ostriker, J. P. 1977, ApJ, 218, 148
Men'shchikov, A., André, P., Didelon, P., et al. 2010, A&A, 518, L103
Micic, M., Glover, S. C. O., Banerjee, R., & Klessen, R. S. 2013, MNRAS, 432, 626
Miyama, S. M., Narita, S., & Hayashi, C. 1987, PThPh, 78, 1051
Molinari, S., Swinyard, B., Bally, J., et al. 2010, A&A, 518, L100
Myers, P. C. 2009, ApJ, 700, 1609
Nagai, T., Inutsuka, S.-I., & Miyama, S. M. 1998, ApJ, 506, 306
Naranjo-Romero, R., Zapata, L. A., Vázquez-Semadeni, E., et al. 2012, ApJ, 757, 58
Ostriker, J. 1964, ApJ, 140, 1056
Padoan, P. 1995, MNRAS, 277, 377
Padoan, P., Juvela, M., Goodman, A. A., & Nordlund, Å. 2001, ApJ, 553, 227
Padoan, P., & Nordlund, Å. 1999, ApJ, 526, 279
Padoan, P., & Nordlund, Å. 2002, ApJ, 576, 870
Padoan, P., & Nordlund, A. 2011, ApJ, 730, 40
Padoan, P., Nordlund, Å., Kritsuk, A. G., Norman, M. L., & Li, P. S. 2007, ApJ, 661, 972
Pavlovski, G., Smith, M. D., Mac Low, M.-M., & Rosen, A. 2002, MNRAS, 337, 477
Peretto, N., Fuller, G. A., André, P., et al. 2014, A&A, 561, A83
Pon, A., Toalá, J. A., Johnstone, D., et al. 2012, ApJ, 756, 145
Schisano, E., Rygl, K. L., Molinari, S., et al. 2014, ApJ, in press (arXiv:1406.4443)
Schneider, N., Csengeri, T., Bontemps, S., et al. 2010, A&A, 520, A49
Smith, R. J., Shetty, R., Stutz, A. M., & Klessen, R. S. 2012, ApJ, 750, 64
Spitzer, L., Jr., & Fitzpatrick, E. L. 1995, ApJ, 445, 196
Tasker, E. J., & Bryan, G. L. 2008, ApJ, 673, 810
Toalá, J. A., Vázquez-Semadeni, E., & Gómez, G. C. 2012, ApJ, 744, 190
Vazquez-Semadeni, E. 2012a, in Magnetic Fields in Diffuse Media, ed. E. de Gouveia dal Pino & A. Lazarian, in press (arXiv:1208.4132)
Vázquez-Semadeni, E. 2012b, EAS Publications Series, Vol. 56, The Role of the Disk-Halo Interaction in Galaxy Evolution: Outflow vs. Infall?, ed. M. A. de Avillez (Cambridge: Cambridge Univ. Press), 39
Vázquez-Semadeni, E., Ballesteros-Paredes, J., & Klessen, R. S. 2003a, ApJL, 585, L131
Vázquez-Semadeni, E., Banerjee, R., Gómez, G. C., et al. 2011, MNRAS, 414, 2511
Vázquez-Semadeni, E., Colín, P., Gómez, G. C., Ballesteros-Paredes, J., & Watson, A. W. 2010, ApJ, 715, 1302
Vázquez-Semadeni, E., Gazol, A., Passot, T., et al. 2003b, in Lecture Notes in Physics, Vol. 614, Turbulence and Magnetic Fields in Astrophysics, ed. E. Falgarone & T. Passot (Berlin: Springer-Verlag), 213
Vázquez-Semadeni, E., Gazol, A., & Scalo, J. 2000, ApJ, 540, 271
Vázquez-Semadeni, E., Gómez, G. C., Jappsen, A.-K., Ballesteros-Paredes, J., & Klessen, R. S. 2009, ApJ, 707, 1023
Vázquez-Semadeni, E., Gómez, G. C., Jappsen, A.-K., et al. 2007, ApJ, 657, 870
Vázquez-Semadeni, E., González, R. F., Ballesteros-Paredes, J., Gazol, A., & Kim, J. 2008, MNRAS, 390, 769
Vázquez-Semadeni, E., Kim, J., Shadmehri, M., & Ballesteros-Paredes, J. 2005, ApJ, 618, 344
Vázquez-Semadeni, E., Ryu, D., Passot, T., González, R. F., & Gazol, A. 2006, ApJ, 643, 245
Vishniac, E. T. 1994, ApJ, 428, 186
Wada, K., & Norman, C. A. 2007, ApJ, 660, 276
Walch, S., Whitworth, A. P., & Girichidis, P. 2012, MNRAS, 419, 760
Walder, R., & Folini, D. 2000, Ap&SS, 274, 343